Real-time detection of virus antibody interaction by label-free common-path interferometry

Samer Alhaddad, Houda Bey, Olivier Thouvenin, Pascale Boulanger, Claude Boccara, Martine Boccara, Ignacio Izeddin

Biophysical Reports

REPORT

Real-time detection of virus antibody interaction by label-free common-path interferometry

Samer Alhaddad,[1] Houda Bey,[1] Olivier Thouvenin,[1] Pascale Boulanger,[2] Claude Boccara,[1] Martine Boccara,[1,3,*] and Ignacio Izeddin[1,*]

[1]Institut Langevin, ESPCI Paris, CNRS, PSL University, Paris, France; [2]Institut de Biologie Intégrative de la Cellule, Université Paris-Saclay, CNRS, CEA, Orsay, France; and [3]Institut de Biologie de l'ENS, CNRS, Inserm, Paris, France

ABSTRACT Viruses have a profound influence on all forms of life, motivating the development of rapid and minimally invasive methods for virus detection. In this study, we present a novel methodology that enables quantitative measurement of the interaction between individual biotic nanoparticles and antibodies in solution. Our approach employs a label-free, full-field common-path interferometric technique to detect and track biotic nanoparticles and their interactions with antibodies. It is based on the interferometric detection of light scattered by viruses in aqueous samples for the detection of individual viruses.We employ single-particle tracking analysis to characterize the size and properties of the detected nanoparticles, and to monitor the changes in their diffusive mobility resulting from interactions. To validate the sensitivity of our detection approach, we distinguish between particles having identical diffusion coefficients but different scattering signals, using DNA-loaded and DNA-devoid capsids of the *Escherichia coli* T5 virus phage.In addition, we have been able to monitor, in real time, the interaction between the bacteriophage T5 and purified antibodies targeting its major capsid protein pb8, as well as between the phage SPP1 and nonpurified anti-SPP1 antibodies present in rabbit serum. Interestingly, these virus-antibody interactions are observed within minutes. Finally, by estimating the number of viral particles interacting with antibodies at different concentrations, we successfully quantify the dissociation constant K_d of the virus-antibody reaction using single-particle tracking analysis.

WHY IT MATTERS The recent health crisis has emphasized the need for innovative approaches to swiftly and accurately detecting viral infections and assessing immune responses. In this study, we introduce a rapid, cost-effective, and reusable experimental setup that allows for the comprehensive characterization of viral particles, antibodies, and their interactions within a sample.

Our method harnesses the advantages of label-free optical interferometry, capitalizing on the specific binding between viral particles and antibodies at low concentrations to enable efficient detection. Notably, this approach facilitates the detection of virus-specific antibodies in serum samples and the determination of their specific affinity to the targeted virus.

In summary, our newly developed system represents a speedy and dependable tool for detecting viral infections and evaluating the host's immune response. Its ability to deliver reliable results while being cost-effective and reusable makes it a valuable asset in combating viral outbreaks.

INTRODUCTION

The rapid and efficient detection and characterization of viruses are critical in preventing the global spread of diseases. Early identification of viruses is particularly important for targeted therapy, expanding treatment options, reducing morbidity, and limiting transmission (1). Consequently, virus detection has garnered significant interest in the biomedical, pharmaceutical, and research fields to promote the development of new testing and diagnosis methods.

Currently, virus detection methods can be broadly categorized into three groups. Firstly, there are techniques based on measuring infectivity by amplifying the virus within its specific eukaryotic or bacterial host. These methods involve mixing serial dilutions of the virus with their host and immobilizing them in

Submitted March 27, 2023, and accepted for publication July 27, 2023.

*Correspondence: martine.boccara@mnhn.fr or ignacio.izeddin@espci.fr

Editor: Jorg Enderlein.

https://doi.org/10.1016/j.bpr.2023.100119

a semisolid growth medium, where a viral plaque indicates infection of cells adjacent to infected cells. Quantification of the infectious virus is then derived from the number of plaque-forming units (PFUs) (2,3). While viral plaque-forming assays serve today as the gold standard, they can be time-consuming, taking up to several days depending on the virus being tested.

Secondly, there are techniques that examine the viral nucleic acid or proteins, such as PCR (polymerase chain reaction) amplification or antigen-based tests. PCR techniques offer high specificity by searching for and amplifying specific genetic material, typically yielding results within a few hours (4). Antigen-based tests, on the other hand, detect the presence of specific viruses in a sample by targeting proteins on the virus surface using antibodies. These tests are cost-effective and provide quick results within tens of minutes (5). However, they are less sensitive and quantitative compared with PCR detection (6).

The third category of virus detection techniques relies on direct optical measurements of viral particles, such as dynamic light scattering. This technique can estimate the average size of viruses and nanoparticles (NPs) in a solution, but they lack sensitivity to detect single viruses. Light microscopy techniques offer a powerful and noninvasive means to study biological samples with potential for high throughput. However, conventional optical systems struggle to directly visualize NPs and virus particles due to their small size and low refractive index difference compared with water, resulting in weak scattering and phase contrasts. Fluorescence microscopy methods have been commonly used to address this limitation, employing fluorescent labels to tag capsid proteins (7) or DNA viral genomes (8). One notable example is flow cytometry, where individual viruses are counted and identified thanks to fluorescence labeling. Recent advances using calcium labeling have also enabled rapid virus detection through modifications in particle diffusion mobility (9). Nonetheless, fluorescence techniques are hindered by phototoxicity and photobleaching. Therefore, label-free optical approaches are more suitable for virus characterization. While all the aforementioned techniques are appropriate for virus titration, for high-resolution analysis of virus morphologies, electronic and atomic force microscopy techniques are well suited (10,11).

In recent years, highly sensitive optical interferometric microscopy techniques have attracted growing attention for their potential to characterize viruses at the single-particle level without the need for labeling. Various configurations of optical setups have been employed for different interferometric microscopy techniques, allowing for the detection, identification, and tracking of small particles, molecules, metallic particles, and other materials in a wide range of applications (12–15) (see (16,17) for recent reviews). These imaging methods have been applied to characterize single particles in solutions (18), as well as sensing and imaging protein interactions sites (19). Interferometric scattering methods can quantify the particle size and scattering strength and have demonstrated excellent sensitivity, even down to detecting single proteins (17,20). However, the lack of specificity in label-free interferometric methods poses a challenge when dealing with structurally similar entities possessing similar optical properties. Different groups have addressed this issue in various ways, from surface functionalization to facilitate selective binding to receptors at specific sites (21,22) to studying protein interactions by monitoring changes in interferometric contrast (23,24).

In our previous work, we showcased the detection, tracking, counting, and differentiation of viruses and vesicles in an aquatic environment (25,26). To accomplish this, we developed a full-field, incoherently illuminated, common-path interferometer operating in transmission, and employed single-particle tracking (SPT) analysis in combination with the interferometric signal's magnitude to distinguish between different populations of particles of similar size but different characteristics. In this study, we have enhanced our system's sensitivity by using a high-speed camera with a high full-well capacity, leading to interferometric contrast improvement. We have also refined our estimation of individual particle diffusion coefficient by adapting an algorithm used for tracking single fluorescent molecules (code available in the supporting material). Consequently, we achieved a threefold increase in sensitivity, enabling the differentiation between empty capsids and DNA-filled capsids of the same virus. More importantly, to make our technique specific to the virus' molecular nature, we have developed a novel assay to monitor changes in scattering and Brownian diffusion upon the addition of specific antibodies. We first demonstrate this approach using purified rabbit IgGs, including polyclonal antibodies targeting the major capsid protein pb8 of phage T5. We also successfully detected the interaction between SPP1 phages and anti-SPP1 antibodies present in rabbit serum. Within approximately 1 min, we observe a signature of the antibodies' reaction with antigens present on the virus capsid, with further aggregation detected within a few minutes. Finally, by evaluating the variation in the number of virus particles interacting with antibodies as a function of the concentration of antibodies in the sample, we quantify the molecular dissociation rate of the virus-antibody reaction.

MATERIALS AND METHODS

Phages, capsids, and antibodies

In this study, we utilized purified T5 phages and SPP1. The T5 virion consists of a 90-nm icosahedral capsid (head) and a flexible, noncontractile tail measuring 250 nm in length. The T5 empty capsid has a well-defined molecular mass of 26.0 MDa, while the filled capsid has a molecular mass of 105.4 MDa (27). The initial concentration of T5 bacteriophages was estimated to be 7.3×10^{12} PFU/mL. We also analyzed full (with DNA) and empty (devoid of DNA) capsids of T5 using our experimental setup. The full capsids had an estimated concentration of 10^{12} heads/mL, while the empty capsids had an initial concentration of 4×10^{13} heads/mL (28,29). Before experiments, phages and capsids were diluted in T5 buffer (10 mM Tris-Cl [pH 7.4], 100 mM NaCl, 1 mM $MgCl_2$).

The SPP1 bacteriophage has a similar morphology to T5 but with a smaller capsid (30). The SPP1 virion consists of an icosahedral, isometric capsid with a diameter of approximately 60 nm and a long, flexible, noncontractile tail. We worked with an initial concentration of 2.24×10^{11} PFU/mL and, before the experiments, the SPP1 viruses were diluted in a buffer composed of 100 mM Tris-Cl (pH 7.5), 100 mM NaCl, and 10 mM $MgCl_2$.

We used purified IgGs from polyclonal serum targeting the T5 major capsid protein (pb8: 775 copies/capsid), which has a concentration of 0.84 mg of protein/mL. The serum containing antibodies against whole SPP1 particles (31,32) was centrifuged at 14,000 rpm for 10 min to remove large aggregates, and we measured a protein concentration of 0.1 mg/mL in the supernatant.

Optical setup and acquisition

In this study, we employed a similar setup for the common-path interferometer as described in (25), with the addition of a new sensor featuring an improved full-well capacity and faster acquisition speed, leading to a significant improvement of the signal/noise ratio. This improvement enables the detection and tracking of smaller viruses with better precision.

Fig. 1 *a* illustrates the schematic drawing of the full-field common-path interferometer. The sample is illuminated by a 455-nm light-emitting diode (LED) (Thorlabs, USA, M455L4, 455 nm, 1150 mW) positioned as close as possible under a coverslip that holds the droplet sample. The LED light passes through the suspension containing NPs, which scatter the light. A water immersion objective lens (100×, NA = 1, Olympus, Tokyo, Japan) is used to collect the light coming from the LED and scattered by the NPs in a transmission configuration. The light is then directed to a tube lens with a focal length of 300 mm, forming an image on the camera placed at its focal distance.

A significant modification in our setup is the introduction of a new camera (Quartz Q-2HFW, Adimec, Eindhoven, the Netherlands) with a maximum frame rate of 720 frames/s at full chip (1440×1440 pixels) and a full-well capacity of 2×10^6 electrons. With this new camera, we observed a threefold improvement in the signal/noise ratio compared with our previous measurements with the optical setup described in (25). The total magnification of our setup, accounting for the objective and tube lens, is 167×, resulting in a field-of-view of 103×103 μm^2 on the sample plane. The use of an incoherent LED is practical as it does not require additional processing to reduce speckle artifacts. In our experimental configuration, we positioned the LED beneath the coverslip at a distance of a few millimeters (1–2 mm). This configuration allows us to underfill the numerical aperture of the objective lens, while still being able to capture the interferometric contrast from NPs.

Unlike most interferometric scattering microscopy setups that typically employ a common-path reflection configuration and laser illumination, we opted for a transmission configuration and utilized an incoherent light source for illumination. While working in a reflection configuration may offer potentially higher interferometric contrast due to the partial reflection of the glass interface (0.4%) attenuating the reference beam, working in a transmission configuration offers greater robustness, ease of use, and the ability to detect NPs in the volume without requiring precise positioning. With the faster acquisition and higher full-well capacity camera in our transmission setup, we achieve not only higher interferometric contrast but also the ability to monitor faster dynamics.

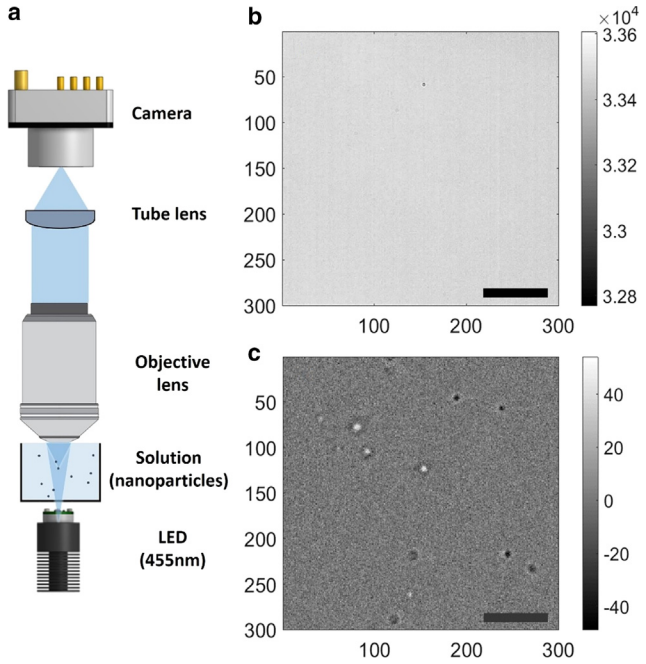

FIGURE 1 Interferometric setup and single-particle interferometric images. (*a*) Schematic of the common-path interferometer setup. The sample is illuminated by an incoherent 455 nm LED with a full angle of 80° (Thorlabs, M455L3). The light passes through the sample solution, and the light coming from the LED as well as the light scattered from the nanoparticles are collected using a water immersion objective lens (Olympus 100×, NA = 1). The collected light is then focused using a tube lens with a focal lens of 300 mm onto an Adimec Quartz Q-2HFW camera. (*b*) Zoomed-in direct image of an unprocessed frame. Scale bar, 5 μm. Images are acquired at 500 FPS with an exposure time of 1.8 ms. (*c*) Processed image, where the stack of frames is normalized to a value of 4000 and the average of the entire stack is subtracted from each frame. Scale bar, 5 μm. The bright and dark spots in the processed image (*c*) represent the point spread functions (PSFs) of 100 nm diameter SiO_2 particles immersed in water.

In a typical experiment, images were acquired at a speed of 500 frames/s. A typical acquisition, corresponding to one time point of diffusion estimation, consisted of 500 images, resulting in a total measurement time of 1 s. For our experiments on virus/antibody interactions, we performed acquisitions in a binary logarithmic scale.

Principle of virus detection and interferometric signal

The measurement modality employed in this study involves capturing the interference signal between the reference field emitted by the light source and the light field scattered by the NPs present in

the liquid. The recorded intensity on a camera pixel can be described by:

$$P_d \propto \left(|\boldsymbol{E}_i|^2 + |\boldsymbol{E}_s|^2 + 2|\boldsymbol{E}_i||\boldsymbol{E}_s|\cos\Delta\phi\right) \quad (1)$$

where P_d represents the power intensity recorded on the camera, $\boldsymbol{E}_i$ is the incident field on the NP, $\boldsymbol{E}_s$ is the scattered electric field, and $\Delta\phi$ denotes the phase difference between the reference electric field and the electric field extinction of the NPs.

In transmission and for small particles such as viruses, the phase difference primarily encompasses Gouy and defocus phase shift, which is caused by variations in the wave vectors at the focal plane of the objective lens, as well as the phase contribution determined by the dielectric function of the nano-object (9). Consequently, constructive and destructive interferences occur depending on the axial position of the particle within the liquid. The scattered field emanating from the particle is proportional to the incident reference field, $\boldsymbol{E}_s \propto \alpha \boldsymbol{E}_i$, where α represents the complex polarizability. In the Rayleigh approximation regime (NP size $<<$ wavelength), $\alpha \propto 3\epsilon_m V\left(\frac{\epsilon_p - \epsilon_m}{\epsilon_p + 2\epsilon_m}\right)$, where ϵ_m and ϵ_p denote the permittivities of the surrounding medium and the particle, respectively, and V indicates the volume of the particle.

For viruses, the scattering field $\boldsymbol{E_s}$ is negligible compared with the incident field $\boldsymbol{E_i}$, and the static background originating from the LED illumination dominates over the scattered and interference terms in Eq. 1. As a result, direct detection of the NPs in suspension is hindered (Fig. 1 *b*). To extract the interference term containing information about the NPs moving in the liquid, we first remove the static background of each frame in the image stack by subtracting the temporal average of the 500 frames from each individual frame (Fig. 1 *c*). A final step in image processing involves removing stripe artifacts caused by line amplification of CMOS sensors. A 1D filter is applied in the Fourier plane to remove these stripes in the image (see supporting material, section 1 for more information).

In contrast to fluorescence imaging, the amplitude of the point spread function (PSF) carries information about the size and the axial position of the scatterer (33). As an illustration, bright and dark spots on the image in Fig. 1 *c* PSF correspond to constructive and destructive interferences, respectively.

SPT analysis

After processing the raw images as described in the previous section, we use a modified version of the multiple-target tracing algorithm (34) typically used for detecting and tracking fluorescent particles. However, since the signals in our experiments can oscillate from negative to positive values due to interference, the algorithm needs to be adapted for interferometric imaging compared with fluorescence imaging. In short, the algorithm steps are the following: 1) detection and fitting of isolated PSFs with a Gaussian function to determine their subpixel position in the image. 2) Trace reconnection: the algorithm determines the most probable reconnection of traces to build trajectories of individual NPs diffusing in the liquid. 3) As a result, we obtain a list of trajectories that contains the subpixel localization of the NP for each time stamp, as well as the amplitude of the interference signal intensity for each localization. For bright and dark detections, the localization is performed in two consecutive steps, and the positions are used interchangeably for the tracking process. The modified code for single-particle detection and tracking code can be found in the supporting material, section 2.

Since the amplitude of the interference signal depends on the axial position of the NPs, we extract the maximum value for each particle during its entire trajectory. This ensures that the NP has explored, by Brownian motion, an intensity maximum that characterizes its scattering behavior.

For each trajectory, we compute the mean-square displacement (MSD) as a function of lag time (Δt). The MSD is given by $MSD(\Delta t) = \langle[\boldsymbol{r}(t+\Delta t) - \boldsymbol{r}(t)]^2\rangle$, where $\boldsymbol{r}(t)$ represents the position of the NP at time t. By analyzing the MSD, we can determine whether the diffusion follows a Brownian behavior and estimate the associated diffusion coefficient. Brownian diffusion is characterized by a linear dependence of the MSD with the lag time Δt. To verify the random nature of the NPs diffusion, we apply a linear fit of the logarithm of each MSD(Δt): $\log(MSD(\Delta t)) = \log(4D) + \beta \log(\Delta t)$, where the β coefficient indicates the diffusion regime of the NPs. For NPs in a liquid suspension, the β coefficient is expected to be 1 for a pure Brownian behavior (35,36). If the distribution of β coefficients is centered around 1, a linear fit is applied to the MSD curves of each trajectory, $MSD(\Delta t) = 4D\Delta t$, to estimate the diffusion coefficient D of the NPs. Also, we have chosen to call the power coefficient β instead of the more common α to avoid confusion with the polarizability parameter.

The diffusion coefficient D is directly related to the hydrodynamic radius of the NP through the Stokes-Einstein relation $D = \frac{K_B T}{6\pi\eta R}$, where K_B is the Boltzmann constant, T is the temperature of the solution, η is the viscosity of the medium, and R the hydrodynamic radius of the NP.

A calibration experiment using SiO_2 NPs with a diameter of 100 nm is presented in the supporting material, section 4. We also tested the setup's performance with SiO_2 NPs of 50 nm in diameter; further details can be found in the supporting material.

Estimation of molecular antibodies' affinity

The virus-antibody reaction is complex due to the numerous possible interaction sites between the viruses and antibodies. Such complex reaction can be characterized by consecutive avalanche reactions, as described in supporting material, section 5. In our approach, we consider each capsid protein on the virus as one antibody binding site (37). Each virus in this case contains 775 binding sites (the number of pb8 capsid proteins). This approximation is valid when the antibodies specifically target a protein on the virus surface.

To describe the system at the equilibrium state, the following saturation equation can be used (37):

$$r = \frac{[Ab]_{bound}}{[V]_0} = \frac{n[Ab]}{K_d + [Ab]} \text{ where } [Ab]_{bound} = n * [V]_{bound} \quad (2)$$

where r is defined as the ratio of interacting viruses over the initial concentration of viruses in the sample, $[Ab]_{bound}$ is the concentration of bound antibodies, n is the number of possible binding sites per virus capsid, $[V]_{bound}$ is the concentration of viruses interacting with at least one antibody, and K_d is the dissociation constant characterizing the affinity of the interaction between antibodies and viruses (37).

The concentration of bound antibodies can be estimated by measuring the number of viral particles that remain *free* in liquid, i.e., with the same diffusion coefficient as the control, until the system reaches its equilibrium as described in Eq. 2. This can be achieved by tracking the changes in diffusion coefficient over time. The concentration of bound viruses can be calculated as $[V]_{bound} = [V]_0 - [V](t)$, where $[V]_0$ is the initial concentration of viruses and $[V](t)$ the concentration of noninteracting viruses at time t.

Since single antibodies are too small to be detected using our optical setup, we rely on tracking the number of interacting viruses over time. To estimate the concentration of bound antibodies, we compare the distribution of measured diffusion coefficients over time with that of the T5 control sample. When a virus interacts with an antibody, its effective hydrodynamic radius increases,

resulting in a slower diffusion coefficient and a larger interferometric signal. Incidentally, this increase of signal leads to a larger volume of detection. Therefore, by normalizing and subtracting the diffusion coefficient histograms of the virus-antibody samples and the control diffusion coefficient histogram, we can determine the percentage of particles that have not interacted with antibodies.

In practice, sedimentation can be neglected in our experiments. The sedimentation rate of 100-nm SiO_2 particles is approximately 10^{-8} m/s (considering the size and density of the particle, the density and viscosity of the surrounding liquid, and gravity), which is significantly slower than the acquisition time of a stack of images (1 s) and the duration of the virus-antibody experiments (1 h).

RESULTS

Sensitivity of the system: Differentiating full versus empty T5 capsids

We have improved the interferometric contrast by a factor of 3 using a camera with an improved full-well capacity (see materials and methods). This enhancement proves to be effective in detecting particles of smaller size and those with a smaller refractive index difference from the surrounding medium. With this improved sensitivity, we used SPT analysis to investigate the ability to differentiate NPs of similar size but different composition. Specifically, we focused on the T5 capsids that can either contain tightly condensed 121 kb dsDNA (full capsids) or devoid of DNA (empty capsids). Although these two populations exhibit similar diffusion coefficients in liquid, we considered that the refractive index of the full capsids would be higher. To explore this, we processed image acquisitions to extract the diffusion characteristics of the particles along with their corresponding interferometric signals.

The ability to distinguish between full and empty virus particles holds significant importance in the fields of molecular therapy and nanomedicine. Recent research has compared the various analytical methods for achieving this differentiation (38). One of the methods described in this review is mass photometry, which employs interferometric scattering microscopy in reflection. Mass photometry relies on comparing the interferometric contrast of individual particles bound to an activated coverslip to distinguish between particles (39). In practice, mass photometry exhibits higher sensitivity in detecting the binding and unbinding of smaller particles based on the interferometric contrast but requires proper activation of the coverslip for the particles of interest.

The approach that we use in our paper combines the estimation of size via the MSD with the measurement of interferometric contrast, which has also recently been reported in a reflection configuration (18). In reflection, the sensitivity is potentially better due to the attenuation of the reference beam, but the volume of detection is limited to a couple of hundred nanometers from the surface of the coverslip.

Initially, we estimated the diffusion coefficient and interferometric intensity for each homogeneous solution of the two populations (Fig. 2, *a* and *b*). Each acquisition was performed at a nominal concentration of 10^9 $\mathrm{particles/mL}$. We found a median diffusion coefficient of 3.92 ± 0.87 $\mu\mathrm{m}^2/\mathrm{s}$ for 192 tracked empty T5 capsids compared with 4.05 ± 0.98 $\mu\mathrm{m}^2/\mathrm{s}$ for 471 tracked full T5 capsids (Fig. 2 *a*). Fig. 2 *b* shows histograms of the maximum interferometric intensity measured for each trajectory. As expected, the average intensity obtained for empty capsids (60.49 $\pm$ 6.25 a.u.) was lower than that obtained for the full capsids (86.38 $\pm$ 9.68 a.u.). This difference in signal explains the lower detection probability of empty capsids compared with full capsids.

These results demonstrate that, despite the similar diffusion properties, interferometric intensity can serve as an indicator to distinguish viruses or NPs of similar size but different refractive index. In addition, we observed a slight difference in the average diffusion coefficient between empty and full capsids, as well as a larger distribution of full capsids compared with empty ones. These findings align with the morphological studies of the capsids conducted using transmission electron microscopy (28).

To further validate the capability of differentiating empty and full capsids in a heterogeneous sample, we conducted a second experiment with a suspension containing both types of capsids at a similar concentration. As expected, we were not able to distinguish between the two populations based on their diffusion coefficient, as shown in Fig. 2 c. When fitting the histogram of diffusion coefficients with two Gaussian distributions using least-squared error fitting, we observed an overlap of the curves, resulting in diffusion coefficients of 3.82 ± 1.9 and $3.77 \pm 1.9 \mu\mathrm{m}^2/\mathrm{s}$ for the two populations. However, we clearly observed a bimodal distribution of the interferometric signal (Fig. 2 *d*). The first population, centered at 58.33 $\mathrm{a.u.}$ with a SD of 8.11 a.u., represents the empty capsids. The second population, centered at 88.03 $\mathrm{a.u.}$ with a SD of 9.75 $\mathrm{a.u.}$, consists of full capsids with higher intensity due to the presence of DNA, which has a higher refractive index.

Importantly, we also acknowledge the presence of a potential bias in our observations when estimating the concentration of virus present in the suspension. Although we used a similar concentration and observed similar diffusion mobility for both empty and full capsids, we tracked approximately 2.5 times more full capsids than empty capsids. This discrepancy can be attributed to the fact that full capsids generate a higher interferometric signal, which enables their detection

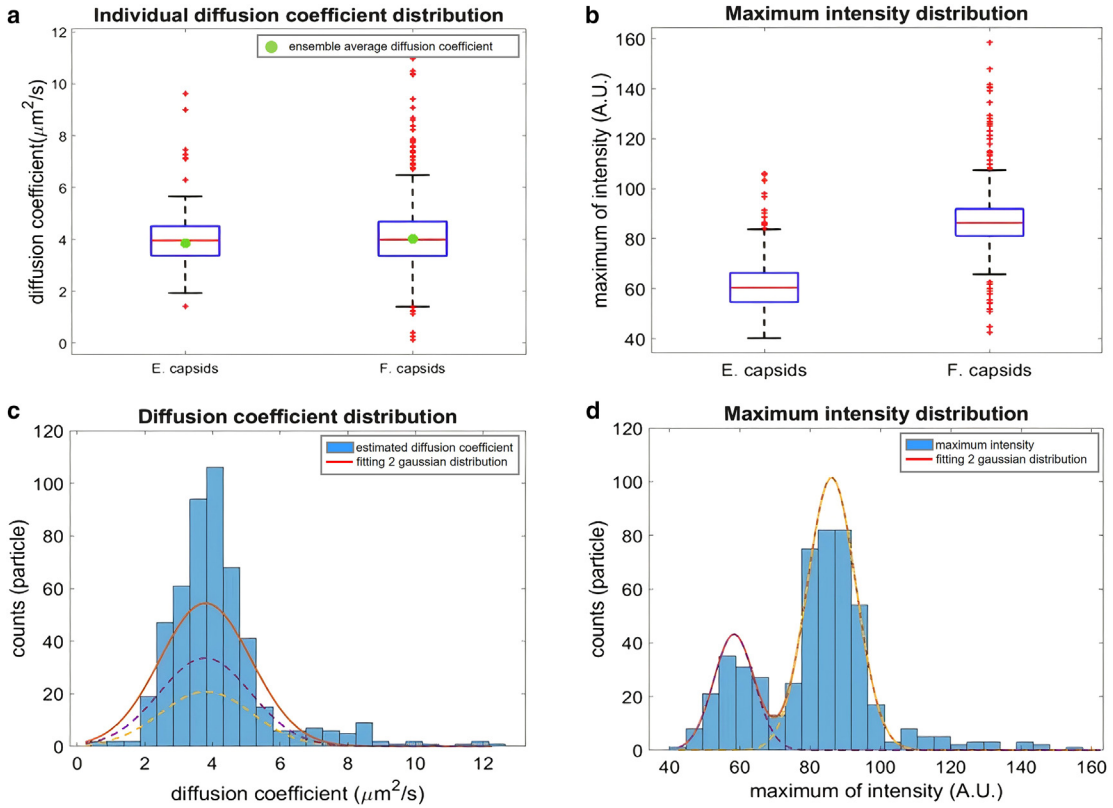

FIGURE 2 Differentiation between full and empty T5 capsids. (*a*) The boxplot shows the distribution of individual diffusion coefficients for both empty and full capsids. For empty capsids the median diffusion coefficient is 3.92 μm^2/s, with the 25th and 75th percentile values ranging between 3.35 and 4.61 μm^2/s. For full capsids, the median diffusion coefficient is 4.05 μm^2/s, with the 25th and 75th percentile values ranging between 3.48 and 4.75 μm^2/s. The ensemble average diffusion coefficients, obtained by fitting the ensemble average MSD, are 3.86 μm^2/s for empty capsids and 4.03 μm^2/s for full capsids. (*b*) The boxplot represents the distribution of maximum of intensity values for empty and full capsids. For empty capsids, the median intensity is 60.49 a.u., with the 25th and 75th percentile values ranging between 54.57 and 66.28 a.u. For full capsids, the median is 86.38 a.u. and the 25th and 75th percentiles are at 81.175 and 91.9 a.u. (*c*) The histogram, fitted with two Gaussian normal distributions, shows the distribution of the estimated diffusion coefficients for a mixture of empty and full capsids. The estimated parameters are as follows: amplitudes (20.85 counts/33.57 counts), mean values (3.82/3.77 μm^2/s), and SDs (1.9/1.9 μm^2/ s). (*d*) The histogram represents the distribution of maximum intensity values. The estimated parameters for the Gaussian fitted distributions are as follows: amplitudes (101.63/43.26 counts), mean values (88.03/58.33 a.u.), and SDs (9.75/8.11 a.u.).

over a larger axial range and at greater distances from the microscope focus.

It is crucial to consider this larger detection volume when precise quantification of virus concentration is required, particularly in our upcoming experiments. By accounting for this bias, we can ensure more accurate measurements and interpretations of the concentration data.

Real-time monitoring of T5-IgG recognition based on changes in diffusion constant

Once we established the sensitivity of our system to measure diffusion coefficients, interferometric signal, and number of detections for individual viruses, we proceeded to design an experiment aimed at assessing the recognition of targeted viruses by antibodies by monitoring changes in these parameters over time.

We initiated the experiment by immersing the objective lens in a droplet containing a diluted solution of purified polyclonal IgG molecules, which contained anti-pb8 antibodies directed toward the major capsid protein of T5 phages. T5 phages were then added to the solution, with each T5 phage possessing about 775 binding sites (pb8 molecules) on its surface. To ensure sufficient antibody coverage, we used an excess ratio of 2000 antibody molecules for each virus in the sample.

Subsequently, we performed acquisitions of 500 images at 500 Hz for each time point after mixing the T5 phages with the IgG solution. It is important to note that our optical system cannot directly detect antibody molecules. The measurements were taken on a binary logarithmic scale to effectively monitor the rapidly varying behavior at the beginning of the measurements series. This scale was applied to T5-IgG

sample, as well as to the two control experiments: phages only and antibodies only.

Fig. 3, *a* and b, illustrate the processed images of T5 phages, respectively, without and in the presence of specific antibodies at different time intervals (see Video S1 for the image sequence of T5 phages interacting with anti-pb8 antibodies). Visual inspection of the T5 control (Fig. 3 *a*) did not reveal any significant differences over time. However, upon adding T5 phages to the antibody solution (Fig. 3 *b*), differences in terms of contrast, number of spots, and size of the detected spots became apparent. These modifications were further confirmed through SPT analysis, as shown in Fig. 3, *c* and *d*.

We observed a progressive decrease in the diffusion coefficient for the sample containing IgG molecules and T5 phages. One minute after adding the T5 phages, a median diffusion coefficient of $3.11 \pm 0.81\ \mu m^2/s$ was obtained. Over time, this value gradually decreased to $1.17 \pm 0.96\ \mu m^2/s$ after 64 min. According to the Stokes-Einstein equation, the hydrodynamic radius of individual particles increases by a factor of 3 within 64 min (see Fig. 3 *c*). This modification of the diffusivity was accompanied by a continuous increase in the interferometric signal, as shown in Fig. 3 *d*. No significant modification in terms of diffusion coefficient or interferometric intensity was detected for the T5-only control (Fig. 3, *c* and *d*).

It is worth noting that we did not detect any aggregation in the IgG control solution (see supporting material for more information). In addition, we conducted another control test by adding T5 phages to purified antibodies against the surface glycoprotein of vesicular stomatitis virus and no differences were detected during the measurement time (available in supporting material, section 7). These results confirm the specificity of the reaction.

The observed increase in hydrodynamic radius and interferometric intensity of the detected NPs confirms the aggregation of the virus particles in the presence of antibodies.

Overall, these results highlight the changes observed in the diffusion coefficient and interferometric intensity as indicators of virus-antibody recognition and the aggregation of virus particles in the presence of antibodies.

Monitoring virus-antibody reaction in physiological serum

In previous sections, we demonstrated the effectiveness of our assay in monitoring the interaction between a specific virus and its corresponding antibodies using Brownian diffusion and SPT analysis. We then aimed to expand our methodology to the more challenging scenario of virus interaction with crude serum, which presents additional complexities due to the presence of various particles and molecules that may not necessarily interfere with the virus. However, these NPs can affect the SPT analysis. Our next experiments focused on the interaction between SPP1 phage and serum containing multiple polyclonal antibodies that target different epitopes displayed on structural proteins of the virus (from SPP1 capsid or tails).

To establish a baseline, we conducted control measurements by separately examining SPP1 phages and the serum solution. Subsequently, we introduced the virus into the serum solution, resulting in a final concentration of $2 \times 10^9\ \mathrm{PFU/mL}$ of SPP1 phages in the serum solution.

As shown in Fig. 3 *e*, we observed a gradual decrease in the diffusion mobility of individual particles in the sample containing SPP1 phages and the anti-SPP1 serum. Over a duration of 32 min, the measured median diffusion coefficient decreased from 3.89 ± 0.89 to $2.79 \pm 0.99\ \mu m^2/s$. At the same time, there was an increase in the average size of the particles, indicated by the increase of the interferometric signal from 72.8 ± 9.5 to 129.6 ± 11.3 a.u. (Fig. 3 *f*). Importantly, the diffusion coefficient and the interferometric signal remained constant over time for both control samples (Fig. 3, *e* and *f*). Despite the presence of various particle types and multiple antibody molecules within the serum, the reaction between the serum and targeted phages was detectable within a few minutes, as evidenced by changes in both the interferometric signal and the estimated diffusion coefficient (Fig. 3, *e* and *f*).

To check the specificity of the virus to antibody reaction in the serum, we investigated the interaction between bovine serum albumin, since serum albumin is the most common protein found in a serum and may have interacted with the virus. We observed no significant changes in the diffusion coefficient after mixing T5 phages and bovine serum albumin at a concentration commonly found in plasma (approximately 50 mg/mL) over a period of 1 h (see supporting material, section 7). We also examined possible interaction between T5 phages and nonimmune rabbit serum, and similarly found that the nonspecific serum had no discernible effect on the trajectories of T5 phages (see supporting material, section 7 for more information).

Altogether, these experiments advocate for the specific interaction between T5 phages and their specific antibodies inside the immune serum as observed in Fig. 3, *e* and *f*.

Quantitative measurements of affinity

While our assay initially provided a qualitative assessment of the interaction between phages and antibodies

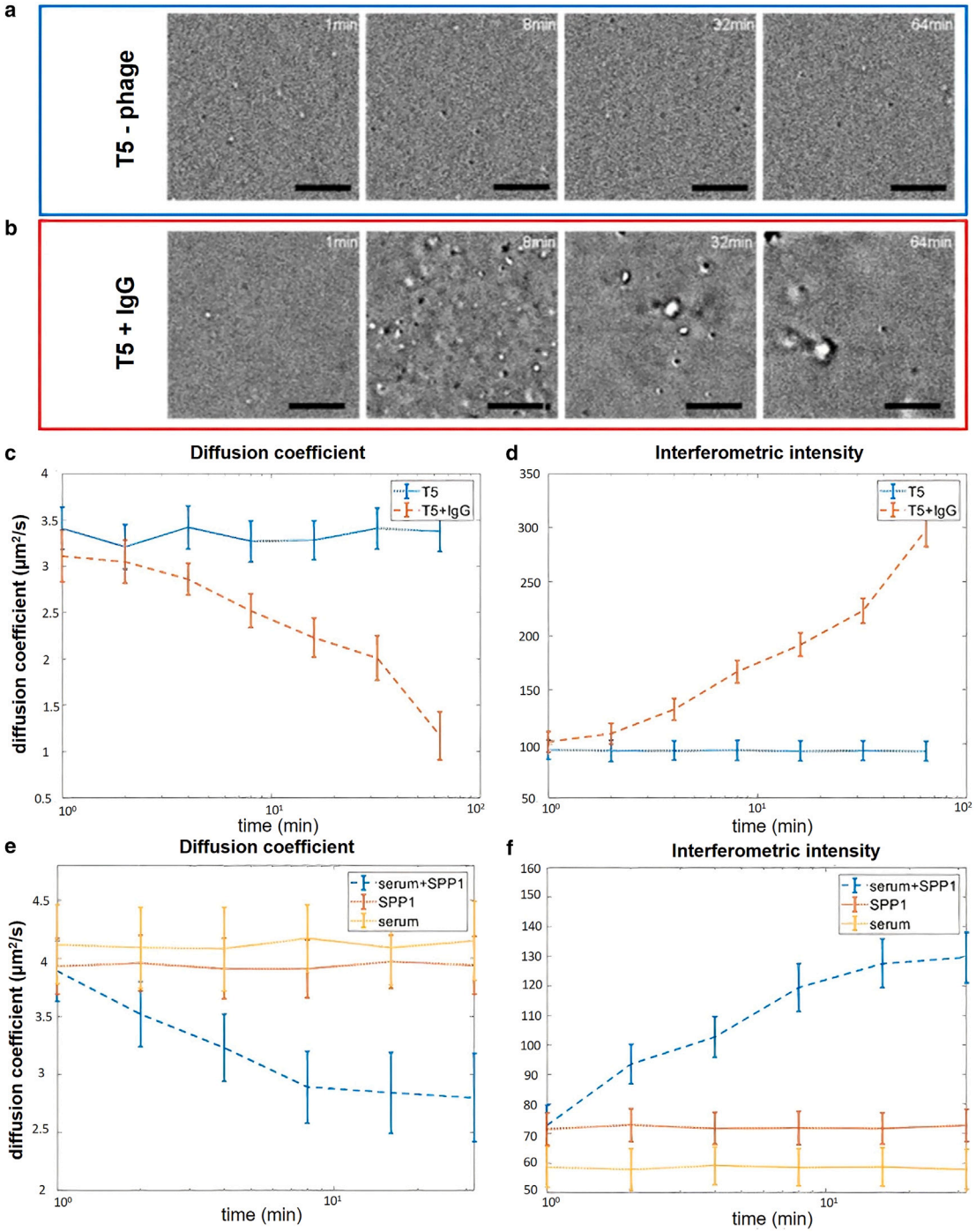

FIGURE 3 Recognition signature between virus-antibodies and viruses-serum. In the top image gallery, snapshots at different time points are shown for the T5 bacteriophages alone (*a*) and the T5 phages in interaction with IgG anti-pb8 (*b*). Scale bars, 5 μm. . A visual inspection reveals that the T5 control exhibits similar PSFs and contrast of single spots, while the size and contrast of spots progressively increase when antibodies are added to the T5 phages. (*c* and *d*) Represent the diffusion coefficient and the maximum intensity, respectively, resulting from SPT analysis of the T5 and the T5 + IgG experiments. The interaction between T5 phages and IgG is evident from the increase of interferometric signal and the progressive decrease in the diffusion coefficient of the particles. (*e* and *f*) Show the diffusion coefficient and the maximum intensity, respectively, of Spp1 + serum as well as the Spp1 alone and serum alone controls, as function of time. These curves result from the progressive aggregation of SPP1 phages and antibodies present in the serum, indicating their interaction.

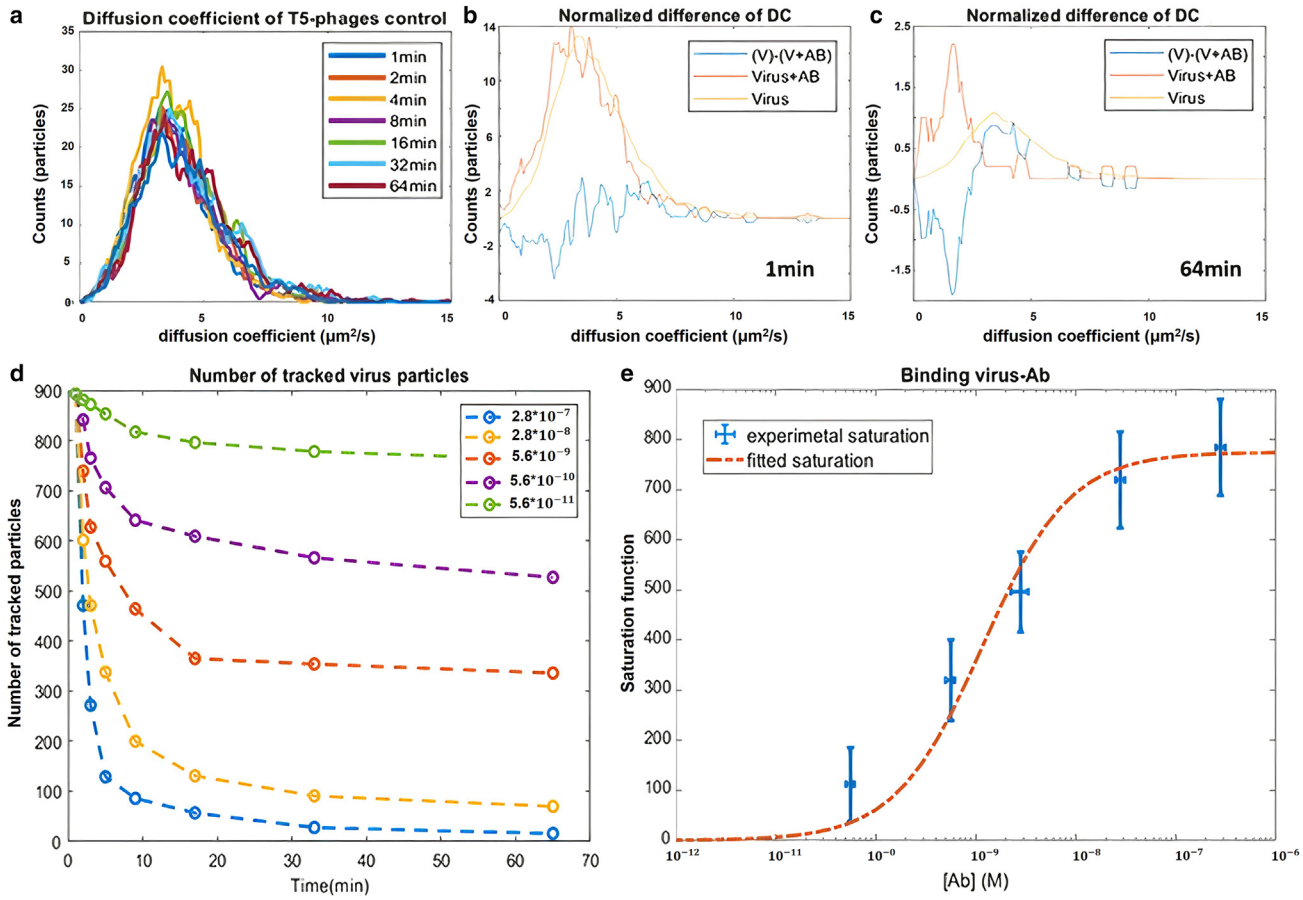

FIGURE 4 Estimation of the K_d constant of the virus-antibodies interaction. (*a*) Histogram of diffusion coefficients of the T5 phage control sample at different time points. (*b*) Normalized diffusion coefficient histograms for the control of T5 and T5 + antibody (Ab), with (*c*) representing the difference between the two curves. (*d*) Number of virus particles tracked in the sample solution at different time intervals while varying the concentration of antibodies (the legend indicates the concentration of antibodies in M). (*e*) Saturation function curve depicting the binding reaction as a function of antibodies concentration in the sample solution.

in a solution, our goal was to extract quantitative measurements of affinity from our data. Specifically, we focused on evaluating the dissociation rate between the phage T5 and polyclonal IgG antibodies targeting the pb8 protein on the T5 capsid. For this purpose, we conducted experiments with varying concentrations of antibodies in the solution. Our objective was to determine, for each initial concentration of antibodies, the number of T5 phages that interact with antibodies over time.

The recognition between viruses and antibodies leads to the aggregation of particles, where larger particles have a higher interferometric contrast and can be detected in a bigger volume of detection compared with individual viruses. By monitoring the variation of individual viruses, we can quantify the aggregation in the same detection volume as the individual T5 viruses. We estimated the number of nonaggregated and aggregated viruses at each time lag by comparing the distribution of the diffusion coefficient of the tracked particles. However, a straightforward comparison in number of particles is not possible due to the variation in the volume of detection. Instead, we compared the ratios of tracked particles, relative to the total number of particles, to determine the fraction of T5 phages that interacted with antibodies. As described in estimation of molecular antibodies affinity, we utilized the change in the number of interacting particles to estimate the quantity of interacting particles in the sample solution.

In Fig. 4 *a*, we display the histogram of diffusion coefficients obtained for the control sample at each time point, confirming their temporal stability. Next, we compare the diffusion coefficient histograms for various antibody concentrations and time intervals to the diffusion coefficient curve of the T5 control sample. Since the addition of antibodies to the virus solution leads to fluctuations in the number of tracked particles across different time intervals, we normalize the diffusion coefficient curves against the control curve, taking

into account the total number of particles. We then calculate the percentage of viruses that retain their initial diffusion coefficient values.

Fig. 4 *b* illustrates the diffusion coefficient histogram curve obtained 1 min after adding the antibodies at a concentration of 0.042 mg/mL, corresponding to 2.8×10^{-7}M. Comparing this curve to the diffusion coefficient histogram curve acquired 64 min after adding antibodies, a clear shift toward smaller diffusion coefficients can be observed (Fig. 4 *c*). Using the estimated ratio derived from the comparison of diffusivity, we can determine the number of viruses that have not yet interacted with antibodies, considering the total number of tracked particles for various antibody dilutions (Fig. 4 *d*).

Fig. 4 *d* illustrates two distinct trends in the number of tracked virus particles that are not interacting with antibodies over time for various antibody concentrations. Initially, the number of detected viruses decreases rapidly within few minutes, followed by an asymptotic behavior indicating that the system has reached its chemical equilibrium. Using the data points at equilibrium at the 64-min time point for various concentrations, we can estimate the number of bound antibodies in the solution. Although tracking virus-antibodies reaction on a molecular scale is complex, the use of the saturation function presented in estimation of molecular antibodies affinity is suitable for estimating the dissociation constant of the reaction. The pb8 capsid protein possesses 775 binding sites (28). Despite the occurrence of various levels of aggregation in the presence of antibodies, our analysis involves a comparison between individual virus particles and aggregated particles, enabling the estimation of the average dissociation rate of the antibodies being utilized.

Fig. 4 *e* displays the saturation function of the binding as function of the concentration of antibodies. By fitting the experimental data using the saturation function expression in Eq. 2, we estimate a dissociation constant $K_d = 1.17 \times 10^{-9}$M. This value falls within the standard range of affinity describing the interaction between viruses and antibodies at equilibrium (40). A lower K_d value indicates a stronger reaction between the two species. So far, we have been interested in the equilibrium state. However, the variation in the number of virus particles in the solution over time can also provide an indication of the reaction speed, as presented in the supporting material, section 5.

CONCLUSION AND DISCUSSION

In this study, we have introduced a novel label-free analysis approach to provide fast, reliable, and reusable detection of biotic NPs, viruses, and antibodies involved in interactions with viruses. Our methodology is based on SPT analysis of NPs in a solution, and we have achieved enhanced performance through improvements in both hardware and software components.

We have demonstrated the ability to differentiate between particles of similar size but with different structures using T5 capsids. This distinction is made possible by relying on both the interferometric signal and the diffusion coefficient of individual particles. This capability holds significant promise for applications in nanomedicine and drug delivery control, as it enables the nondestructive monitoring of the load of small vector viruses (39).

The limit of detection of our method is determined by two main factors: the number of data points and the selected tracking parameters. The number of data points corresponds to the tracked particles using specific tracking parameters, as described in the supporting material, section 8. The average mean estimated value is dependent on the amount of data used, while the dispersion error is influenced by the chosen tracking parameters. To improve the limit of detection, two strategies can be employed. Firstly, increasing the measurement time, which increases the number of data points. Secondly, accepting a higher dispersion error can also enhance the limit of detection. In our study, we employed a chosen particle concentration to ensure an adequate number of data points during a 1-s acquisition time, thus enabling accurate estimation. It is worth noting that particles with higher interferometric contrast generally have a lower limit of detection, as they can be detected over a larger volume during the acquisition. Another approach to enhance the limit of detection in a transmission interferometric microscope is by attenuating the reference beam collected by the camera detector, thereby increasing the interferometric contrast of specific particles. Such attenuation would give similar results as a reflection configuration (19), where the reference beam is only partially reflected by the coverslip.

Using SPT analysis, we have successfully detected the recognition signature between viruses and specific antibodies, in purified solution and in immune serum. This signature is characterized by a progressive increase in the interferometric signal and a decrease in the diffusion coefficient of individual spots. We observed this recognition signature within the first few minutes of adding specific antibodies to a virus-containing solution. Furthermore, our approach allows for the estimation of the dissociation rate of specific antibodies. By analyzing the trajectories obtained from SPT, we can estimate a molecular dissociation rate of species in their initial form, without significant manipulation of the initial species. The speed of aggregation in this context is influenced by the concentration

of viruses and antibodies in the sample. The estimation of the dissociation rate is conducted once the system reaches equilibrium. For a given antibody concentration, the dissociation constant (K_d) can be estimated, regardless of the reaction speed, which depends on the initial virus concentration in the sample.

It is important to note that, despite the nonspecificity of the label-free virus detection technique used in this study, which detects all sorts of NPs in a nonpurified solution such as serum, our measurements rely on changes of diffusion coefficient and interferometric signal. These changes over time are the signature of the recognition between viruses and antibodies.

In conclusion, our study successfully demonstrates the ability to detect the recognition signature between viruses and nonpurified serum containing multiple NPs and proteins without the need for sophisticated sample processing. A simple centrifugation step of a few minutes is sufficient to remove large aggregates from the serum. The use of nonpurified serum highlights the potential of our approach as a rapid and straightforward method for diagnostic tests targeting specific viruses or the presence of specific antibodies.

SUPPORTING MATERIAL

Supplemental information can be found online at https://doi.org/10.1016/j.bpr.2023.100119.

AUTHOR CONTRIBUTIONS

S.A. conceived the original idea for the virus-antibody reaction monitoring method outlined in this paper. S.A., M.B., and I.I. collaborated on the design of the experiments and the data analysis approach. P.B. prepared the biological samples of viruses, capsids, and antibodies. S.A. and M.B carried out the experiments and data analysis, with H.B. providing assistance on some experiments. C.B. aided in designing the optical setup and contributed to our understanding of signal amplification and origin. O.T. played a part in the approach to K_d quantification. The paper was written by S.A., M.B., and I.I., and then revised by all authors.

ACKNOWLEDGMENTS

We extend our gratitude to Yves Gaudin, Aurélie Albertini, Paulo Tavares, and Odon Thiébeauld for the biological samples. This work was supported by the European Union's Horizon 2020 under the Marie Skłodowska-Curie grant (no. 754387) and the French National Research Agency ("Agence National de la Recherche"; Project-ANR-19-CE18-0028).

DECLARATION OF INTERESTS

The authors declare that they have no known competing financial interests or personal relationships that could have appeared to influence the work reported in this paper.

REFERENCES

1. Lotfi, M., M. R. Hamblin, and N. Rezaei. 2020. COVID-19: Transmission, prevention, and potential therapeutic opportunities. *Clin. Chim. Acta.* 508:254–266. https://doi.org/10.1016/j.cca.2020.05.044.
2. Baer, A., and K. Kehn-Hall. 2014. Viral Concentration Determination Through Plaque Assays: Using Traditional and Novel Overlay Systems. *JoVE.* 93, 52065. https://doi.org/10.3791/52065.
3. Price, A. A., T. R. Sampson, …, D. S. Weiss. 2015. Cas9-mediated targeting of viral RNA in eukaryotic cells. *Proc. Natl. Acad. Sci. USA.* 112:6164–6169. https://doi.org/10.1073/pnas.1422340112.
4. Kehl, S. C., and S. Kumar. 2009. Utilization of Nucleic Acid Amplification Assays for the Detection of Respiratory Viruses. *Clin. Lab. Med.* 29:661–671. https://doi.org/10.1016/j.cll.2009.07.008.
5. Benirschke, R. C., E. McElvania, …, S. Das. 2019. Clinical Impact of Rapid Point-of-Care PCR Influenza Testing in an Urgent Care Setting: a Single-Center Study. *J. Clin. Microbiol.* 57. e01281-18. https://doi.org/10.1128/JCM.01281-18.
6. Pray, I. W., L. Ford; …, CDC COVID-19 Surge Laboratory Group. 2021. Performance of an Antigen-Based Test for Asymptomatic and Symptomatic SARS-CoV-2 Testing at Two University Campuses — Wisconsin, September–October 2020. *MMWR Morb. Mortal. Wkly. Rep.* 69:1642–1647. https://doi.org/10.15585/mmwr.mm695152a3.
7. Curry, A., H. Appleton, and B. Dowsett. 2006. Application of transmission electron microscopy to the clinical study of viral and bacterial infections: Present and future. *Micron.* 37:91–106. https://doi.org/10.1016/j.micron.2005.10.001.
8. Kuznetsov, Y. G., and A. McPherson. 2011. Atomic Force Microscopy in Imaging of Viruses and Virus-Infected Cells. *Microbiol. Mol. Biol. Rev.* 75:268–285. https://doi.org/10.1128/MMBR.00041-10.
9. Bönisch, I. Z., L. Dirix, ..., Z. Debyser. 2020. Capsid-Labelled HIV To Investigate the Role of Capsid during Nuclear Import and Integration. J. Virol. 94: e01024-19. https://doi.org/10.1128/JVI.01024-19.
10. Brandenburg, B., and X. Zhuang. 2007. Virus trafficking – learning from single-virus tracking. *Nat. Rev. Microbiol.* 5:197–208. https://doi.org/10.1038/nrmicro1615.
11. Robb, N. C., J. M. Taylor, …, A. N. Kapanidis. 2019. Rapid functionalisation and detection of viruses via a novel Ca2+-mediated virus-DNA interaction. *Sci. Rep.* 9, 16219. https://doi.org/10.1038/s41598-019-52759-5.
12. Ignatovich, F. V., and L. Novotny. 2006. Real-Time and Background-Free Detection of Nanoscale Particles. *Phys. Rev. Lett.* 96, 013901. https://doi.org/10.1103/PhysRevLett.96.013901.
13. Ewers, H., V. Jacobsen, …, V. Sandoghdar. 2007. Label-Free Optical Detection and Tracking of Single Virions Bound to Their Receptors in Supported Membrane Bilayers. *Nano Lett.* 7:2263–2266. https://doi.org/10.1021/nl070766y.
14. Daaboul, G. G., A. Yurt, …, M. S. Ünlü. 2010. High-Throughput Detection and Sizing of Individual Low-Index Nanoparticles and Viruses for Pathogen Identification. *Nano Lett.* 10:4727–4731. https://doi.org/10.1021/nl103210p.
15. Huang, Y.-F., G.-Y. Zhuo, …, C.- L. Hsieh. 2017. Label-free, ultrahigh-speed, 3D observation of bidirectional and correlated intracellular cargo transport by coherent brightfield microscopy. *Nanoscale.* 9:6567–6574. https://doi.org/10.1039/C7NR00604G.
16. Taylor, R. W., and V. Sandoghdar. 2019. Interferometric Scattering Microscopy: Seeing Single Nanoparticles and Molecules via Rayleigh Scattering. *Nano Lett.* 19:4827–4835. https://doi.org/10.1021/acs.nanolett.9b01822.
17. Priest, L., J. S. Peters, and P. Kukura. 2021. Scattering-based Light Microscopy: From Metal Nanoparticles to Single Proteins. *Chem. Rev.* 121:11937–11970. https://doi.org/10.1021/acs.chemrev.1c00271.

18. Kashkanova, A. D., M. Blessing, …, V. Sandoghdar. 2022. Precision size and refractive index analysis of weakly scattering nanoparticles in polydispersions. *Nat. Methods.* 19:586–593. https://doi.org/10.1038/s41592-022-01460-z.

19. Olerinyova, A., A. Sonn-Segev, …, P. Kukura. 2021. Mass Photometry of Membrane Proteins. *Chem.* 7:224–236. https://doi.org/10.1016/j.chempr.2020.11.011.

20. Dahmardeh, M., H. M. Dastjerdi, …, V. Sandoghdar. 2022. Self-supervised machine learning pushes the sensitivity limit in label-free detection of single proteins below 10 kDa. *In* Review. https://doi.org/10.21203/rs.3.rs-1635524/v1.

21. Park, J.-S., I. B. Lee, …, M. Cho. 2018. Label-free and live cell imaging by interferometric scattering microscopy. *Chem. Sci.* 9:2690–2697. https://doi.org/10.1039/C7SC04733A.

22. Piliarik, M., and V. Sandoghdar. 2014. Direct optical sensing of single unlabelled proteins and super-resolution imaging of their binding sites. *Nat. Commun.* 5:4495. https://doi.org/10.1038/ncomms5495.

23. Soltermann, F., W. B. Struwe, and P. Kukura. 2021. Label-free methods for optical *in vitro* characterization of protein–protein interactions. *Phys. Chem. Chem. Phys.* 23:16488–16500. https://doi.org/10.1039/D1CP01072G.

24. Gutgsell, A. R., A. Gunnarsson, …, S. Geschwindner. 2022. Biosensor-Enabled Deconvolution of the Avidity-Induced Affinity Enhancement for the SARS-CoV-2 Spike Protein and ACE2 Interaction. *Anal. Chem.* 94:1187–1194. https://doi.org/10.1021/acs.analchem.1c04372.

25. Boccara, M., Y. Fedala, …, A. C. Boccara. 2016. Full-field interferometry for counting and differentiating aquatic biotic nanoparticles: from laboratory to Tara Oceans. *Biomed. Opt Express.* 7:3736–3746. https://doi.org/10.1364/BOE.7.003736.

26. Roose-Amsaleg, C., Y. Fedala, …, M. Boccara. 2017. Utilization of interferometric light microscopy for the rapid analysis of virus abundance in a river. *Res. Microbiol.* 168:413–418. https://doi.org/10.1016/j.resmic.2017.02.004.

27. Wu, D., P. Hwang, …, G. Piszczek. 2021. Rapid Characterization of AAV gene therapy vectors by Mass Photometry. *Biophysics*. https://doi.org/10.1101/2021.02.18.431916.

28. Dominguez-Medina, S., S. Fostner, …, S. Hentz. 2018. Neutral mass spectrometry of virus capsids above 100 megadaltons with nanomechanical resonators. *Science.* 362:918–922. https://doi.org/10.1126/science.aat6457.

29. Huet, A., R. L. Duda, …, J. F. Conway. 2019. Capsid expansion of bacteriophage T5 revealed by high resolution cryoelectron microscopy. *Proc. Natl. Acad. Sci. USA.* 116:21037–21046. https://doi.org/10.1073/pnas.1909645116.

30. Huet, A., J. F. Conway, …, P. Boulanger. 2010. In *Vitro* Assembly of the T=13 Procapsid of Bacteriophage T5 with Its Scaffolding Domain. *J. Virol.* 84:9350–9358. https://doi.org/10.1128/JVI.00942-10.

31. Lhuillier, S., M. Gallopin, …, S. Zinn-Justin. 2009. Structure of bacteriophage SPP1 head-to-tail connection reveals mechanism for viral DNA gating. *Proc. Natl. Acad. Sci. USA.* 106:8507–8512. https://doi.org/10.1073/pnas.0812407106.

32. Vinga, I., C. Baptista, …, C. São-José. 2012. Role of bacteriophage SPP1 tail spike protein gp21 on host cell receptor binding and trigger of phage DNA ejection: SPP1 tail spike protein binding to the YueB receptor. *Mol. Microbiol.* 83:289–303. https://doi.org/10.1111/j.1365-2958.2011.07931.x.

33. Auzat, I., A. Dröge, …, P. Tavares. 2008. Origin and function of the two major tail proteins of bacteriophage SPP1. *Mol. Microbiol.* 70:557–569. https://doi.org/10.1111/j.1365-2958.2008.06435.x.

34. Gholami Mahmoodabadi, R., R. W. Taylor, …, V. Sandoghdar. 2020. Point spread function in interferometric scattering microscopy (iSCAT). Part I: aberrations in defocusing and axial localization. *Opt Express.* 28:25969–25988. https://doi.org/10.1364/OE.401374.

35. Sergé, A., N. Bertaux, …, D. Marguet. 2008. Dynamic multiple-target tracing to probe spatiotemporal cartography of cell membranes. *Nat. Methods.* 5:687–694. https://doi.org/10.1038/nmeth.1233.

36. Michalet, X. 2010. Mean square displacement analysis of single-particle trajectories with localization error: Brownian motion in an isotropic medium. *Phys. Rev. E.* 82, 041914. https://doi.org/10.1103/PhysRevE.82.041914.

37. Michalet, X., and A. J. Berglund. 2012. Optimal diffusion coefficient estimation in single-particle tracking. *Phys. Rev. E.* 85, 061916. https://doi.org/10.1103/PhysRevE.85.061916.

38. Bisswanger, H. 2017. Enzyme kinetics: principles and methods, 3rd, enlarged and improved. Wiley-VCH.

39. Saha, K., F. Bender, and E. Gizeli. 2003. Comparative Study of IgG Binding to Proteins G and A: Nonequilibrium Kinetic and Binding Constant Determination with the Acoustic Waveguide Device. *Anal. Chem.* 75:835–842. https://doi.org/10.1021/ac0204911.

40. Werle, A. K., T. W. Powers, …, H. A. Runnels. 2021. Comparison of analytical techniques to quantitate the capsid content of adeno-associated viral vectors. *Mol. Ther. Methods Clin. Dev.* 23:254–262. https://doi.org/10.1016/j.omtm.2021.08.009.